Author Manuscript

Author Manuscript

Author Manuscript

Author Manuscript

HHS Public Access

Author manuscript

Acta Biomater. Author manuscript; available in PMC 2024 June 01.

Published in final edited form as:

Acta Biomater. 2023 June ; 163: 312–325. doi:10.1016/j.actbio.2022.02.023.

Mechanical strain in the mouse astrocytic lamina increases after exposure to recombinant trypsin☆

Arina Korneva[a,b,*], **Elizabeth C. Kimball**[a], **Sarah Quillen**[a], **Joan L. Jefferys**[a], **Manasi Nawathe**[c], **Yik Tung Tracy Ling**[d], **Thao D. Nguyen**[b,d,e], **Harry A. Quigley**[a,b]

[a]Glaucoma Center of Excellence, Johns Hopkins Wilmer Eye Institute, United States

[b]Department of Ophthalmology, School of Medicine, Johns Hopkins University, Baltimore, MD 21218, United States

[c]Department of Chemical and Biomolecular Engineering, Johns Hopkins University, Baltimore, MD 21218, United States

[d]Department of Mechanical Engineering, Johns Hopkins University, Baltimore, MD 21218, United States

[e]Department of Materials Science, Johns Hopkins University, Baltimore, MD 21218, United States

Abstract

The responses of astrocytes in the optic nerve head (ONH) to mechanical and biochemical stimuli are important to understanding the degeneration of retinal ganglion cell axons in glaucoma. The ONH in glaucoma is vulnerable to stress produced by the intraocular pressure (IOP). Notably, after three days of elevated IOP in a mouse model, the junctions between the astrocytic processes and the peripapillary sclera were altered and the structural compliance of the ONH increased. In order to simulate this aspect of glaucomatous remodeling, explanted mouse eyes were treated with TrypLE, a recombinant trypsin enzyme. Treatment with TrypLE caused the periphery of the astrocytic lamina to contract radially by 0.044 ± 0.038. Transmission electron microscopy showed that TrypLE caused a separation of the end-feet of the astrocyte processes from the basement membrane at the junction with the sclera. Inflation testing after treatment with TrypLE caused an increased strain response in the astrocytic lamina compared to the strain response before treatment. The greatest increase was in the radial Green-Lagrange strain, E_{rr} = 0.028 ± 0.009, which increased by 340%. The alterations in the microstructure and in the strain response of the astrocytic lamina reported in mouse experimental glaucoma were partially reproduced by experimental treatment of mouse eyes with TrypLE. The results herein suggest that separation of junctions between the astrocyte processes and the sclera may be instrumental in increasing the structural compliance of the ONH after a period of elevated IOP.

☆Part of the Special Issue on the Mechanics of Cells and Fibers, guest-edited by Professors Amrinder S. Nain, Derrick Dean, and Guy M. Genin.

*Corresponding author at: Johns Hopkins University, Baltimore, MD 21218, United States. akornev1@jhmi.edu (A. Korneva).

Declaration of Competing Interest

The authors declare that they have no known competing financial interests or personal relationships that could have appeared to influence the work reported in this paper.

Supplementary materials

Supplementary material associated with this article can be found, in the online version, at doi:10.1016/j.actbio.2022.02.023.

Author Manuscript Author Manuscript Author Manuscript Author Manuscript

Keywords

Recombinant trypsin; Glaucoma; Digital volume correlation; Intraocular pressure; Optic nerve head

1. Introduction

Astrocytic glial cells support the retinal ganglion cell axons in the optic nerve head (ONH). In a mouse eye, the tissue in the center of the ONH is comprised largely of astrocytes and is thus sometimes called the astrocytic lamina (AL). In addition, there are capillaries, microglia, and axons of retinal ganglion cells. In larger mammals, astrocytes envelop connective tissue beams to provide mechanical support to axons exiting the eye. Intraocular pressure (IOP) applies stress circumferentially to the AL via the expansion of the scleral canal, and the difference between the IOP and the optic nerve (ON) pressure applies a pressure gradient across the ONH. The astrocytes of this unmyelinated portion of the ON are unique in the central nervous system in that they are subjected to translaminar mechanical stress. In the mouse eye, some individual astrocytes in the unmyelinated region of the ONH can span the entire AL in the coronal plane [1]. The processes of the astrocytes are anchored by dense junctional complexes to the basement membrane of the peripapillary sclera (PPS) [2]. The astrocytes in the mouse AL occupy as much as 80% of tissue volume. Their processes are composed primarily of F-actin and of intermediate filaments, such as glial fibrillary acidic protein (GFAP), vimentin, and nestin [3].

In human glaucoma and in animal models of glaucoma, long-term IOP elevation produces axon damage initially at the ONH [4–6]. We hypothesize that this injury to axons occurs in part from the mechanical strains affecting ONH astrocytes. Studies of the ONH astrocytes in experimental glaucoma have reported changes to astrocyte microstructure, biochemical signaling, gene expression, and function [3,7–14]. We developed an ocular explant model to measure the change in the mechanical behavior of the mouse ONH resulting from acute and chronic IOP elevation [7]. Measurement of the mechanical response of the ONH after chronic IOP elevation demonstrated that changes to the strain response evolve over time, with an initial increase in the compliance of the strain response to IOP increase followed by a transition to lower compliance at a later timepoint [15]. Astrocyte processes also separated from the ONH basement membrane early in the time course of chronic IOP elvation, but were again attached to the basement membrane six weeks after induction of the IOP elevation [2]. To simulate this important aspect of glaucomatous remodeling in a non-IOP dependent model, we considered treating mouse eyes with trypsin, which is widely used for dissociation of cultured cells from the extracellular matrix [16]. In one study, a collagen gel containing cells was treated with trypsin, which led to the dissociation of all cells from the gel without a change in the collagen content [17].

Trypsin is extracted from animal tissue, usually from porcine pancreas, and therefore may contain additional proteases. TrypLE is a trypsin-like protease prepared from recombinant bacteria expressing a microbial protease. TrypLE proteolytic activity is similar to, but not identical to that of trypsin [18,19]. In two studies, TrypLE and trypsin dissociated

Author Manuscript Author Manuscript Author Manuscript Author Manuscript

comparable numbers of cells and did not affect cell viability [20,21]. Therefore, TrypLE was selected in this study in order to simulate astrocyte separation from the ONH basement membrane and the sclera. Astrocyte separation from the ONH basement membrane has been reported in experimental glaucoma, although we recognize that this was not caused by trypsin or TrypLE *in vivo* [2]. We hypothesized that reproducing a feature of glaucoma, albeit artificially by TrypLE, would allow examination of the induced changes in the mechanical response of the ONH and PPS when performing inflation testing of explanted mouse eyes. We treated explanted mouse eyes with TrypLE and buffer for one hour and compared the effect on the astrocyte microstructure using both laser scanning and electron microscopy. We hypothesized that the reduction of astrocyte attachment to the ONH basement membrane and the PPS would increase the strain response of the AL in a manner similar to that observed in a mouse model of glaucoma.

2. Methods

2. 1. Animal studies

All experimental procedures were approved and monitored by the Johns Hopkins University School of Medicine Animal Care and Use Committee. Mice were bred from the FVB/N-Tg(GFAPGFP)14Mes strain [22], whose initial breeding pair was purchased from Jackson Laboratories (#003257). Mice with the allele $Gfap^{GFP}$ express green fluorescent protein under the *Gfap* promoter, which distributes freely within the cytoplasm of all astrocytes, and therefore will be abbreviated by GFP^{Astro}. Both $Gfap^{GFP/WT}$ and $Gfap^{WT/WT}$ mice, of both sexes, and aged 3–8 months old, were used. Mice were euthanized by intraperitoneal injection of ketamine-xylazine-acepromazine solution (ketamine 50 mg/kg, Fort Dodge Animal Health, Fort Dodge, IA; xylazine 10 mg/kg, VedCo Inc., Saint Joseph, MO; acepromazine 2 mg/kg, Phoenix Pharmaceuticals, Burlingame, CA). Mouse eyes were given a topical anesthetic, proparacaine hydrochloride, eye drops (0.5% Akorn Inc. Buffalo Grove, IL, USA). After confirming euthanasia, eyes were enucleated immediately, but the globe remained intact without removal of any internal contents. The experiments were conducted at room temperature. The optic nerve was cut from the eye globe with a razor blade at the level of the posterior sclera to expose the AL. The corneas were glued (Loctite super glue gel control, Henkel Corp., Ohio, USA) to a holder, and the anterior chamber cannulated with a 32-gage needle. The needle was connected to a pressurized phosphate buffered saline (PBS) reservoir column to regulate IOP. The reservoir column was calibrated with a pressure transducer, Omega PX409 0–15psig with 0.08% best straight-line accuracy (Omega Engineering, CT, USA). The holder and eye were situated in a custom bath with PBS. The first step of all *ex vivo* experimental procedures began with eyes at the baseline IOP of 10 mmHg. At the end of *ex vivo* procedures, the eyes were fixed immediately in 4% paraformaldehyde (PFA) for two hours, with IOP maintained at 10 mmHg with a pressurized column of 4% PFA. Fixed eyes were stored in 0.1 M sodium phosphate buffer at 4 °C until processing for fluorescence of F-actin or for transmission electron microscopy (TEM).

Eyes were treated as part of the overall protocol for one hour with either TrypLE or buffer, during which the IOP was maintained at 10 mmHg. TrypLE solution was 1x TrypLE™ Express (Gibco 12604013, no phenol red, in Dulbecco's PBS 0.05% EDTA) and the buffer

Author Manuscript Author Manuscript Author Manuscript Author Manuscript

solution was Dulbecco's PBS (Gibco 14190144, no phenol red, no calcium, no magnesium). When not treated, eyes were kept in a bath of PBS. TrypLE solution contains a recombinant protease which cleaves lysine and arginine peptide bonds on the cell surface similar to the activity of trypsin [18,19]. The experimenter was masked to the identity of the treatment solution during the experiment and during analysis.

A total of 32 eyes were used in the study (Fig. 1, Fig. 2). These eyes were subjected to different *ex vivo* experimental procedures and different processing steps after fixation. Of the 32 eyes, 8 eyes ($n = 4$ buffer, $n = 4$ TrypLE) were from *Gfap*$^{WT/WT}$ mice and were treated *ex vivo,* but not inflation-tested, and after fixation were processed only for TEM. The other 24 eyes ($n = 11$ buffer, $n = 13$ TrypLE) were from both *Gfap*$^{WT/WT}$ and *Gfap*$^{GFP/WT}$ mice, and were subjected to the entire inflation testing protocol (Fig. 1, Fig. 2). Of the 24 eyes, 8 eyes ($n = 3$ buffer, $n = 5$ TrypLE) were from *Gfap*$^{WT/WT}$ mice and after fixation were processed only for fluorescence of F-actin, and 16 eyes ($n = 8$ buffer, $n = 8$ TrypLE) were from *Gfap*$^{GFP/WT}$ mice. These 16 eyes were imaged by second harmonic generation (SHG) and two photon fluorescence (TPF) scans during the inflation testing protocol for analysis of a) the lamina area, b) GFP^{Astro} process network, and c) the strain response in the PPS and AL. After fixation, 10 of the 16 eyes ($n = 6$ buffer, $n = 4$ TrypLE) were used for fluorescence of F-actin and the rest ($n = 2$ buffer, $n = 4$ TrypLE) were not processed further. In summary, 16 eyes ($n = 8$ buffer, $n = 8$ TrypLE) were used in the analysis of the lamina area, GFP^{Astro} process network, analysis of deformation of the AL by treatment, and the strain response. After fixation, 18 eyes ($n = 9$ buffer, $n = 9$ TrypLE) were used in fluorescence analysis of the F-actin network and 8 eyes ($n = 4$ buffer, $n = 4$ TrypLE) were used in analysis of the microstructure with TEM.

2.2. Inflation testing

Twenty-four eyes ($n = 11$ buffer, $n = 13$ TrypLE) from both *Gfap*$^{WT/WT}$ and *Gfap*$^{GFP/WT}$ mice were subjected to the entire inflation testing protocol (Fig. 2). Inflation testing was performed in PBS, by raising the pressure to 10, then to 30 mmHg, with equilibration for 15 min after each pressure step (Fig. 2). Pressure was lowered to 10 mmHg and equilibrated for 15 min. Next, the bath solution was replaced with either buffer (Dulbecco's PBS) or TrypLE. TrypLE is effectively deactivated by dilution with PBS. Therefore, after treatment for one hour, the bath was replaced thrice with PBS with two minutes between washes. Throughout the treatment and washing, the IOP was maintained at 10 mmHg. The eyes then were inflated for the second time with the same timed inflation protocol, from 10 to 30 mmHg.

Out of the 24 eyes, 16 eyes ($n = 8$ buffer, $n = 8$ TrypLE) were from *Gfap*$^{GFP/WT}$ mice and were imaged throughout the experimental protocol. These were all eyes with fluorescent astrocytes in their AL. The mouse ONH has no significant connective tissue and consists of a network of astrocytes through which a modest number of capillaries pass. By AL we will refer to the zone in which astrocytes express GFP (GFP^{Astro}) or in which astrocyte processes are labeled by phalloidin for F-actin. The AL is immediately surrounded by connective tissue of the sclera and pia mater and here this will be called the ONH boundary. The microscope used was a Zeiss two-photon laser scanning microscope 710 with nonlinear

Author Manuscript Author Manuscript Author Manuscript Author Manuscript

optics (LSM 710 NLO, Carl Zeiss Microscopy, LLC, Thornwood, NY), a custom inverted arm, a 20x W Plan Apochromat objective of numerical aperture 1.0, and a Chameleon Ultra II multiphoton laser source (Coherent Inc., Santa Clara, CA). Signals were detected with a Chroma multi band-pass filter (390–410 nm and 470–550 nm, Chroma Technology, Bellows Falls, VT). To visualize the AL the detector collected the TPF signal from excitation at 895 nm. To visualize the collagen and elastin fibers of the ONH boundary formed by the PPS and pia mater, the detector collected SHG and TPF signals from two-photon excitation at 780 nm. The resultant images of the AL were 30–50 μm z-stacks with the resolution of $0.415 \times 0.415 \times 1\ \mu m^3$. The resultant images of the PPS were 40–100 μm z-stacks with a smaller zoom and thus with a lower resolution of $0.519 \times 0.519 \times 1\ \mu m^3$.

Previously, Nguyen et al. reported that the faster the scanning speed the smaller the effect of tissue creep [7]. Therefore, the fastest available scanning speed was used to acquire images before and after treatment for strain measurement with digital volume correlation (DVC) (Section 2.7) and additional measurement of AL area and ONH area (Fig. 2). The fastest scanning speed was limited by the amount of time the laser dwells over a pixel, which was 0.64μs pixel dwell time. Slower scanning speeds improved the resolution of the processes expressing GFP^{Astro} and were used to characterize the astrocyte process network. The slower scans were taken before the treatment step and after the treatment and wash steps (Fig. 2). The slower scans were acquired with a pixel dwell time of 3.15μs and included 2-line averaging.

2.3. Histochemistry for F-actin

After the entire inflation testing protocol, 18 eyes were cryopreserved for histochemistry of F-actin. The eyes were first fixed in 4% PFA with IOP maintained at 10 mmHg. Among the 18 eyes, 8 eyes ($n = 3$ buffer, $n = 5$ TrypLE) were from $Gfap^{WT/WT}$ mice and 10 eyes ($n = 6$ buffer, $n = 4$ TrypLE) were from $Gfap^{GFP/WT}$ mice. Fixed eyes were cryo-preserved in optimal cutting temperature compound (Andwin Scientific TSE TEK CMPND, Thermo Fisher Scientific NC9159334). After initial fixation, the anterior globe and lens were removed leaving the posterior globe intact with the ONH. The fixed posterior globe was cryo-preserved in ascending concentrations of sucrose in 0.1 M PO_4 buffer followed by embedding in 2 parts 20% sucrose buffer to 1 part optimal cutting temperature compound (Andwin Scientific TSE TEK CMPND, Thermo Fisher Scientific NC9159334). Samples were frozen with 2-methylbutane cooled in dry ice and stored at −80 ° C until sectioning on a cryostat. Twelve micron cross-sections of the preserved tissue were made through the tissue sample, yielding between 1 and 7 usable AL sections per eye. The shape of the cross-section of the ON, the morphology of astrocyte processes, and the F-actin network vary along the *z*-axis of the ON. An expert in mouse ON anatomy selected consecutive sections which contained the ONH region. Approximately the same region was imaged during the *ex vivo* inflation testing protocol. Sections were incubated for one hour together with AlexaFluor™ 568 phalloidin for F-actin (1:50, Invitrogen A12380) and with DAPI to label cell nuclei (1:10,000, Roche 10–236–276–001). Sections were imaged with the LSM 710 NLO and Plan-Apochromat 20x/0.8 M27 Zeiss objective. The images were acquired with 2-line averaging, a resolution of $0.160 \times 0.160\ \mu m^2$, and size of $327 \times 327\ \mu m^2$, with two-channel acquisition: 561 nm for phalloidin and 405 nm for DAPI.

Author Manuscript Author Manuscript Author Manuscript Author Manuscript

2.4. Process network image analysis

Quantification of the network of astrocyte processes was performed using the images of the phalloidin-labeled sections and separately using GFP^{Astro} images obtained from the slow LSM scans acquired during inflation experiments (Fig. 2). GFP^{Astro} images, but not the phalloidin fluorescence images, were processed with deconvolution software, Huygens Essential (Scientific Volume Imaging, The Netherlands). All subsequent analysis was performed with MATLAB (version R2019a, MathWorks, Inc., Natick, MA). In order to only analyze the AL, a boundary was drawn in each image. For GFP^{Astro} images, the boundary was drawn automatically to enclose the GFP^{Astro} signal by Otsu's thresholding after Gaussian filtering (*graythresh)* [23]. For actin images, the boundary was manually drawn with the polygon tool (MATLAB, *roipoly*), since an automatic code could not be implemented to correctly exclude the ON sheath and the PPS tissue from the immunofluorescence images.

Next, both GFP^{Astro} and actin image sets were processed and the network of astrocyte process was characterized by the algorithm developed by Ling et al. [3,24]. The algorithm was used as previously described, except the Frangi filter was applied after contrast enhancement, but before binarization in order to improve detection of glial processes [25]. Briefly, the algorithm by Ling et al. uses the median filter (*medfilt2)* and contrast-limited adaptive histogram equalization (*adapthisteq)* to enhance the contrast of processes in the AL. The algorithm binarizes the image (*imbinarize*) such that the detected processes are shaded white and everything else black. The area of GFP^{Astro}-expressing or actin-labeled processes equals the area of the binarized processes (white). Dividing this by the overall AL area yields the area percentage of GFP^{Astro} or actin. To measure the width of processes, a one-pixel wide skeleton was created from the binarized processes by erosion using the function *bwmorph* (MATLAB). The edge-to-edge distance of the binarized process was calculated at each point on the skeleton from the intersections of a line normal to the skeleton to the edges of the binarized processes. The process width was calculated as the mean of the edge-to-edge distances at all points on the skeleton.

2.5. Measurement of the AL and ONH areas

Images acquired during the *ex vivo* inflation testing protocol were used to measure the area of the AL and of the ONH in 16 eyes. These were calculated separately, since it was not assumed that the limit of the fluorescent astrocyte processes and the connective tissue boundary around them were coincident in their two imaging methods or that they would be altered similarly by TrypLE treatment. As mentioned above, the AL area was derived from TPF images and the ONH area from SHG images. The '*merge channels*' tool in FIJI was used to create a two-channel image where the green channel was from the TPF image and the gray channel was from the SHG image [26]. The TFP or SHG images were acquired from fast scans at the baseline 10 mmHg IOP during the before-treatment and the after-treatment inflation tests (Fig. 2). Area from the image before-treatment was compared to the area after-treatment. In the mouse eye, the unmyelinated portion of the ONH begins at the level of the choroid and sclera and continues for 100 μm outside the sclera. Our explant studies were performed after removal of all but the innermost portion of this unmyelinated segment, including some tissue just protruding beyond the scleral surface. Therefore, the

Author Manuscript Author Manuscript Author Manuscript Author Manuscript

GFP^{Astro} (TPF) z-stacks of the AL in general did not coincide with the location of the ONH boundary (SHG) images. To assure that matching positions of both tissues were studied, we used only the overlapping portions of the SHG and TPF z-stacks, which were available in 14 of the 16 imaged eyes (7 buffer-treated and 7 TrypLE-treated), based on the *x, y*, and *z* positions of the microscope stage during their respective acquisition. In the other 2 (n = 1 buffer-treated, n = 1 TrypLE-treated) the TPF z-stack was acquired posterior to the SHG z-stack.

The AL and ONH boundaries were traced manually in FIJI using the polygon tool [26]. To delimit the AL perimeter, the outer-most edge of the fluorescence signal from astrocyte processes was traced. A sensitivity study of the AL area compared the means and standard deviations (std) when 40, 30, 20, 10, and 3 evenly spaced z-slices were used. The study found that the mean and std did not vary significantly when 3 or more z-slices were used. Therefore, the AL was manually traced in the 1st, 21st, and the 41st z-slice, and their mean lamina area was computed. The ONH boundary was marked at the inner edge of the sclera and pia mater where their collagenous tissues have a clear white border in SHG images. In z-stacks that included the entering retinal blood vessels in an inferior, notch-like area, we excluded this vascular stalk from ONH area.

2.6. Transmission electron microscopy (TEM)

TEM was performed on 8 eyes (n = 4 buffer, n = 4 TrypLE) from *Gfap*$^{WT/WT}$ mice. The purpose of these examinations was to optimize ultrastructural preservation, while comparing the specific effects of TrypLE on astrocytes and their relationship to the immediately adjoining connective tissue. Therefore, eyes were explanted just as in the full inflation testing, the ON was transected at the level of the sclera to expose the AL, without removal of any internal tissues or sclera. The specimens were exposed to either buffer or TrypLE for one hour with the IOP maintained at 10 mmHg by the cannula in the anterior chamber as in inflation testing. No inflation tests to IOP of 30 mmHg nor multiphoton imaging of the explants were performed. Eyes were then fixed in 4% PFA, with IOP maintained at 10 mmHg, the posterior pole of fixed eyes was cut at the limbus to remove the lens, the vitreous humor, and the anterior chamber, then placed into 0.1 M sodium phosphate buffer (pH 7.2) for 3 min, then into 0.1 M cacodylate buffer for 1 min, and then into 2% PFA/2.5% glutaraldehyde in cacodylate buffer for 7 min. Samples were placed in 1% osmium tetroxide for 2 h and then dehydrated in ascending ethanol concentrations for 15 min each (50%, 70%, 80%, 95%, 100%). Sections were stained in 1% uranyl acetate in 100% ethanol for 1 hour. The posterior poles were embedded in epoxy resin mixture at 60°C for 48 h. One μm thick sections were used to identify the ONH area in order to study the same anatomical region with TEM as in the rest of this study. Leica EM UC7 ultramicrotome (Leica Microsystems Inc, IL, USA) was used to section tissue into 68 nm, ultrathin sections, which were placed on copper grids and stained with uranyl acetate and lead citrate. Sections were imaged with the Hitachi H7600 microscope (Hitachi High Technologies, Clarksburg, MD) with Advanced Microscopy Techniques Imaging Cameras (Woburn, MA) by an investigator masked to whether the tissue had been treated with buffer or TrypLE.

Author Manuscript Author Manuscript Author Manuscript Author Manuscript

Since the known effects of TrypLE include effects on the attachment of cells to an underlying substrate, we evaluated the effect of treatment on regionally specific features of AL astrocytes that we identified recently [2]. Astrocytes have a dense junctional complex bordering the cell membrane facing their basement membrane. We graded these junctional complexes on a scale from 1 being normal to 4 being most abnormal. The junctional complexes received a grade in three categories: 1) the thickness of the junctional complexes (thinner being abnormal), 2) astrocyte cell membrane (and its junctional complex) having an increased separation from the astrocyte basement membrane (1=astrocyte cell membrane directly next to the basement membrane, 4=maximum separation), and 3) junctional complex continuity (1=continuous complex everywhere facing the basement membrane side to 4=complex absent in many areas (see Fig. 7). Grades were made on multiple tissue sections per sample, with particular attention to the periphery of the AL. The grades were made based on multiple hours of TEM observation. The grades were statistically analyzed by the Mann-Whitney U tests (Section 2.8).

2.7. Strain calculation from image correlation

Images from fast scans acquired during the *ex vivo* inflation testing protocol were used to measure the strain of the AL and of the PPS in 16 eyes (n = 8 buffer-treated and n = 8 TrypLE-treated). We used the SHG and TPF fast scans acquired during the inflation test before treatment and again during the inflation test after treatment (Fig. 2). Image contrast was enhanced by deconvolution (Huygens Essential, Scientific Volume Imaging, The Netherlands), and then by contrast-limited adaptive histogram equalization [26] as described previously [15]. Then, pairs of images from the same eye before and after inflation to 30 mmHg were correlated by an open-source DVC algorithm developed by Bar-Kochba et al. [27,28]. The outputs of the DVC calculation were a field of the image cross-correlation coefficient and the displacement field $\boldsymbol{u}(\boldsymbol{x})$. The image cross-correlation coefficient indicates the degree with which the grayscale intensities can be matched between subset volumes in the reference and the deformed images. The displacement field was smoothed in MATLAB (version R2019a, MathWorks, Inc., Natick, MA) as previously described [15]. The smoothed $\boldsymbol{u}(\boldsymbol{x})$ was applied to calculate the deformation gradient, $\mathbf{F} = (\nabla \boldsymbol{u} + \mathbf{I})$ and the Green-Lagrange strain tensor, $\mathbf{E} = 1/2\,(\mathbf{F}^{\mathrm{T}}\,\mathbf{F} - \mathbf{I})$, where $\mathbf{I}$ is the identity tensor. The outcomes of the strain calculations were the normal strain components, E_{xx}, E_{yy}, E_{zz}, the in-plane shear strain, E_{xy}, the in-plane maximum principal, E_{max}, the in-plane minimum principal, E_{min} , and the in-plane maximum principal shear, γ_{max}. The x, y, and z-directions corresponded to the anatomical nasal-temporal, inferior-superior, and nerve axes, respectively. Cylindrical strain components, E_{rr}, $E_{\theta\theta}$, and $E_{\theta z}$, were computed by transforming the strain tensor $\mathbf{E}$ from the Cartesian coordinate system.

DVC was applied to four sets of z-stacks for each eye to compute the strain response of: 1) the AL before treatment, 2) the AL after treatment, 3) the PPS before treatment, and 4) the PPS after treatment. For each case, the strain tensor was calculated by correlating the deformed z-stack acquired at 30 mmHg to the reference z-stack acquired at 10 mmHg, immediately preceding the 30 mmHg step. Additionally, DVC was used to calculate the effect of buffer versus TrypLE treatment on structure of the AL. For this analysis, DVC was applied to correlate the z-stack acquired at 10 mmHg before treatment to the z-stack

Author Manuscript Author Manuscript Author Manuscript Author Manuscript

acquired at 10 mmHg after treatment for eyes in each treatment group. The resulting DVC deformation indicates the local changes to the configuration of the AL caused solely by treatment with buffer or with TrypLE.

2.8. Statistical analysis

A normal distribution of the data could not be assumed because of the small sample size in this study. Therefore, nonparametric statistical tests were used. Mann-Whitney U (Wilcoxon rank sum) tests were used to compare unpaired measurements across treatment groups, i.e., measurements made on different eyes. The Mann-Whitney U tests (two-tailed) were used to compare the TEM grades (Section 3.4), the radial expansion, and the circumferential expansion of the AL (Table 2) in the buffer group to those in the TrypLE group. The Mann-Whitney U tests (two-tailed) were also used to compare measures of the GFP^{Astro} processes (Table 3), and of the F-actin processes (Table 4) after-buffer to those after-TrypLE.

The Wilcoxon signed rank tests were used to compare paired measurements within a treatment group, i.e., measurements made on the same eye. The values in the buffer group were tested independently from the values in the TrypLE group. The Wilcoxon signed rank tests (two-tailed) were used to compare the AL area, the ONH area (Table 1), measures of the GFP^{Astro} processes (Table 3), the AL strain (Table 5), and PPS strain (Table 6) before treatment to those after treatment. In addition, the Wilcoxon signed rank test (two-tailed) was used to test whether the AL area was statistically different from the ONH area, using the area measurements before treatment.

Values of the radial expansion, circumferential expansion, and strain of the AL were computed by averaging across the whole image volume, across the central region, or across a combined peripheral and rim region. The regions were based on the in-plane radial distance from the centroid to the boundary of the AL. The 0–50% of the radial distance defined the central region, the 50–90% defined the peripheral, and the 90–100% defined the rim. Fewer points correlated by DVC in the rim than in the rest of the AL, therefore combining the peripheral and rim regions was necessary. The combined region was 50–100% of the radial distance to the AL centroid.

Strain differences were computed by subtracting the value before treatment from the value after treatment, with either buffer or TrypLE, e.g., $\Delta E_{rr} = E_{rr,\ after} - E_{rr,\ before}$. The Mann-Whitney U tests (two-tailed) were used to compare the strain differences due to buffer to those due to TrypLE (Tables S6, S7, S12). The regional differences in strain were computed between the central region and the combined peripheral and rim region. In equation form, (central – combined)/(*abs*(combined))*100% where *abs* takes the absolute value, and the combined refers to the strain in the combined peripheral and rim region (Table S10). The Wilcoxon signed rank tests (two-tailed) were used to compare the central to peripheral percent differences before treatment to those after treatment. Statistical tests were performed using SAS version 9.4 (SAS Institute, Cary, NC) or GraphPad Prism version 8 (GraphPad Software Inc., La Jolla, California).

Author Manuscript Author Manuscript Author Manuscript Author Manuscript

3. Results

3.1. Effect of treatment on the AL area

The untreated mean AL area defined by the GFP^{Astro} signal was 11% smaller than the mean ONH area defined by the inner boundary of the SHG signal ($p<0.0002$, $n = 15$) (Fig. 3, Table 1). Buffer treatment did not produce any change in either AL area or ONH area, while TrypLE treatment significantly decreased both AL and ONH areas (−10.8 and −9.9%, respectively, $p \leq 0.03$; Table 1).

3.2. Deformation of the AL by treatment at baseline IOP 10 mmHg

We next used DVC to compare the change in the structure of the astrocytic network of the AL at 10 mmHg before the initial inflation to that after initial inflation and treatment with either buffer or TrypLE (before the second inflation test). Note that this differs from the measurement of strain induced by a change in the inflation pressure. The deformation of the AL due to treatment with buffer was a modest expansion in the radial direction (Fig. 4, Table 2). In contrast, the deformation of the AL due to treatment with TrypLE was a large negative radial expansion, - 0.029 ± 0.027, (i.e., a radial contraction of 0.029 ± 0.027) that was significantly different from the negligible radial expansion due to buffer, 0.005 ± 0.007 ($n = 8$ per group, $p = 0.007$). The modest expansion in the circumferential direction caused by TrypLE, 0.006 ± 0.017 did not differ significantly from that caused by buffer, 0.014 ± 0.013 ($n = 8$, $p = 0.40$).

The effect of buffer and TrypLE was also analyzed regionally (Section 2.8). The radial expansion caused by buffer did not differ by region (Table S1). In contrast, treatment by TrypLE produced a large radial contraction in the combined peripheral and rim regions, 0.044 ± 0.038, that was significantly larger in the comparison with the buffer group, 0.002 ± 0.016 ($n = 8$, $p = 0.007$; Table 2). The small change in the central region did not differ between the TrypLE and buffer treatment groups ($n = 8$ per group, $p = 0.44$).

3.3. Effect of treatment on the GFP^{Astro} and F-actin processes

The mean width of processes expressing GFP^{Astro} was 2.56 ± 0.10 μm and the mean area occupied by the GFP^{Astro} processes (Section 2.4) was 0.013 ± 0.003 mm^2 before treatment with buffer ($n = 8$) (Fig. 5, Table 3). The mean width of the GFP^{Astro} processes calculated for the central, peripheral, and rim regions did not differ statistically ($n = 16$, $p = 0.84$, Figure S2 and Table S2). The GFP^{Astro} process network area occupied 38.8% ± 4.1% of a total area of 0.033 ± 0.007 mm^2 ($n = 8$, Fig. 5).

The width of GFP^{Astro} processes was statistically unchanged by treatment with buffer or with TrypLE (Fig. 5, Table 3). Treatment with buffer caused a 6.1% decrease in total AL area; from 0.033 ± 0.007 mm^2 before treatment to 0.031 ± 0.006 mm^2 after treatment ($n = 8$, $p = 0.02$). Treatment with TrypLE caused a more dramatic decrease in AL area of 12.9%; from 0.031 ± 0.003 mm^2 before treatment to 0.027 ± 0.002 mm^2 after treatment ($n = 8$, $p = 0.0001$). As a result, the GFP^{Astro} Area% after treatment with TrypLE, 41.5 ± 3.3%, was greater than before treatment, 37.2% ± 4.3% ($n = 8$, $p = 0.0006$). The GFP^{Astro} Area% after

Author Manuscript Author Manuscript Author Manuscript Author Manuscript

treatment with buffer was not statistically different than before treatment, even though the total area was statistically smaller.

The mean width of F-actin processes was 1.53 ± 0.11 μm and the mean area occupied by F-actin processes (Section 2.4) was 0.0219 ± 0.0017 mm^2 in fluorescent tissue sections from samples treated with buffer ($n = 9$) (Fig. 6, Table 4). The F-actin filament network occupied the 66.3 ± 0.6% of a total area of 0.033 ± 0.003 mm . There were no statistically significant differences between buffer- and TrypLE-treated specimens in the width of F-actin processes, the area percentage of F-actin processes, and the total AL area ($n = 9$ each). The total AL area in samples treated with TrypLE, 0.030 ± 0.004 mm^2, was 9% smaller than in samples treated with buffer, 0.033 ± 0.003 mm^2, but the comparison was not statistically significant ($p = 0.14$, $n = 9$ each).

3.4. TEM observations after treatment with TrypLE

Ultrastructural observations of the AL and ONH boundary zone were made in two zones: the zone immediately adjacent to the choroid and to the inner scleral contact with the ON; and the zone near where the ON was cut. The latter area was exposed directly to the TrypLE solution, while the former zone was only exposed to protease which diffused across the tissue. In general, the cellular structure of astrocytes was similar in the buffer- and TrypLE-treated specimens and showed no signs of astrocytic toxicity due to treatment. We focused on details of the contact zone between the astrocyte basement membrane, the astrocytic cell membrane, and the dense junctional complexes in the immediate submembrane position facing the basement membrane. An expert masked to the treatment group graded images on a scale of 1=normal to 4=most abnormal in three categories: 1) junctional complex thickness, 2) increased separation between astrocyte cell membrane and the basement membrane, and 3) continuity of the junctional complex along the inner cell membrane. The TrypLE-treated specimens were significantly more abnormal than buffer-treated specimens ($p = 0.022$ by Mann-Whitney U, Fig. 7). Of the 24 possible gradings, the TrypLE-treated specimens had 11 grades of 3 or 4, while buffer-treated had only 3 grades of 3.

3.5. Effect of TrypLE treatment on the strain response of the AL

Inflation from 10 to 30 mmHg caused the AL to stretch biaxially. For the AL before either buffer or TrypLE treatment, the strain in the nasal-temporal direction E_{xx} was two to three times the strain in the inferior-superior direction E_{yy} ($p<0.0001$, $n = 16$, Fig. 8, Table 5, S5). Similarly, the strain in the circumferential direction $E_{\theta\theta}$ was three to four times the strain in the radial direction E_{rr} ($p<0.0001$, $n = 16$). Before treatment with TrypLE or buffer, E_{rr}, E_{xx}, E_{yy}, and E_{min} were at least 150% greater than in the combined peripheral and rim regions. After treatment with TrypLE, all of the in-plane AL normal strain components (E_{rr}, $E_{\theta\theta}$, E_{xx}, E_{yy}), the maximum principal strain E_{max}, and the minimum principal strain E_{min} exhibited large increases after treatment by TrypLE (Table 5). The pairwise comparisons before and after TrypLE treatment were significant for all strain components except $E_{\theta\theta}$ ($n = 8$, $p \leq 0.04$). The largest increase was measured for E_{rr} (340%) while the smallest was for $E_{\theta\theta}$ (21%). The in-plane shear strains ($E_{r\theta}$, E_{xy}, γ_{max}) and the out-of-plane strain (E_{zz}) were unaffected by TrypLE ($n = 8$, $p \geq 0.38$). In contrast, pairwise comparisons of the strain response before and after treatment by buffer were not significantly different ($n = 8$, $p \geq$

Author Manuscript Author Manuscript Author Manuscript Author Manuscript

0.08). The largest increase calculated for E_{rr} after buffer treatment was 34%, which was much smaller than the 340% increase calculated for E_{rr} after TrypLE treatment.

The differences in the strain response after treatment from that before treatment were compared between the TrypLE and buffer groups (Fig. 8). The differences for all 6 strain outcomes caused by TrypLE treatment exceeded the differences in the strain response caused by buffer treatment. The comparisons between the TrypLE and buffer groups were statistically significant for ΔE_{rr}, ΔE_{xx}, ΔE_{yy}, ΔE_{max}, and ΔE_{min} ($n = 8$ per group, $p \leq 0.02$), but not statistically significant for $\Delta E_{\theta\theta}$ ($n = 8$, $p = 0.06$, Table S6). The maximum statistically significant increase caused by TrypLE was ΔE_{rr}, 0.021 ± 0.009, and the minimum was ΔE_{yy}, 0.018 ± 0.010. The ΔE_{rr} and ΔE_{yy} caused by TrypLE were statistically greater than the maximum increase in the strain response caused by buffer, ΔE_{rr}, 0.003 ± 0.004 ($n = 8$ per group, $p \leq 0.001$, Table S7). Treatment in TrypLE produced greater increases in the r- than θ-direction and greater in the y- than x-direction.

The strain response was averaged within the central region and within the combined peripheral region; the latter combined the periphery and the rim of the AL. In the combined peripheral and rim regions, four strain outcomes E_{rr}, E_{xx}, E_{yy}, and E_{min} increased by at least 93% after treatment with TrypLE. The pairwise comparisons before and after TrypLE treatment were significant for six strain outcomes, E_{rr}, $E_{\theta\theta}$, E_{xx}, E_{yy}, E_{max} and E_{min} ($n = 8$, $p<0.04$, Table S9). In contrast, in the central region the pairwise comparisons before and after TrypLE were not statistically significant ($n = 8$, $p \geq 0.31$). Treatment with TrypLE decreased, but did not eliminate the regional variations in the strain response. Before treatment with TrypLE or buffer, six strain outcomes E_{rr}, $E_{\theta\theta}$, E_{xx}, E_{yy}, E_{max} and E_{min} in the central region were at least 48% greater than in the combined peripheral region (Table S10). After treatment with TrypLE, the $E_{\theta\theta}$ and the E_{max} in the central region were greater than in the combined peripheral region by only 14% and 7%, respectively. The percent differences between the central and combined peripheral regions were smaller after treatment with TrypLE than before treatment for $E_{\theta\theta}$, E_{xx}, E_{yy}, and E_{max} ($n = 8$, $p \leq 0.03$), but not statistically different for E_{rr} or E_{min}. For example, before treatment with TrypLE the E_{yy} was 650% ± 570% greater in the central region than in the combined peripheral and rim regions, but after treatment with TrypLE, the E_{yy} was 49% ± 42% greater in the central than in the combined peripheral and rim regions ($n = 8$, $p<0.01$).

3.6. Effect of TrypLE treatment on the strain response of the PPS

Inflation from 10 to 30 mmHg caused both local zones of tension and compression in the PPS. The average maximum and minimum principal strains for the $n = 8$ specimens were $E_{max} = 0.0141 \pm 0.0092$ and $E_{min} = -0.0103 \pm 0.0092$ (Table 6). The strain outcomes in the PPS were between four to ten times smaller than the strain outcomes in the AL. The pairwise comparisons before and after TrypLE treatment were significant for $E_{\theta\theta}$ ($n = 8$, $p = 0.02$), but not for E_{rr} ($n = 8$, $p = 0.20$). The pairwise comparisons before and after TrypLE treatment were significant for the three principal strains (E_{max}, E_{min}, γ_{max}, $n = 8$, $p \leq 0.04$). After TrypLE treatment, $E_{\theta\theta}$, E_{max}, and γ_{max} were at least 27% greater than before treatment, and the magnitude of E_{min} was 88% larger than before treatment. The difference in the strain response after treatment from that before treatment (ΔE) was compared between

Author Manuscript Author Manuscript Author Manuscript Author Manuscript

the TrypLE and buffer groups. The comparisons between the TrypLE and buffer groups were not statistically significant for the 7 strain differences ($n = 8$ per group, $p \geq 0.10$, Table S12).

4. Discussion

Treatment with TrypLE led to both structural and mechanical changes that indicated its major effects were in the AL periphery. TrypLE caused a radial contraction of 0.044 (4%) in the combined peripheral and rim regions, and caused the AL to contract by 10.8%. The density of astrocyte processes expressing GFP^{Astro} increased by approximately 11.5%, but the mean width of the processes was unchanged by this treatment. Altogether these findings suggest that the astrocytes retracted from the more peripheral regions of the ONH. Indeed, the TEM observations show that the astrocyte cell membranes significantly separated from the basement membrane, with concomitant alteration in submembrane junctional complexes. While our findings support the hypothesis that astrocyte alterations affect the strain response, alterations of other tissue elements may also contribute to the outcomes. These features may include TrypLE-induced changes in the scleral extracellular matrix.

The compliance of the strain response to a pressure elevation by 20 mmHg increased after treatment with TrypLE. The radial strain, E_{rr}=0.028 ± 0.009, increased the most, by 370% after TrypLE-treatment. The effect of TrypLE treatment on the strain response of the AL was most dramatic in the periphery. The peripheral effect of in the strain response was consistent with the findings of changes to the attachments of astrocyte processes to the basement membrane. The baseline strain response of a mouse AL to inflation is not uniform, but varies across the AL, as demonstrated here and previously [15]. There is tensile strain in the central region, while there is compressive strain in the peripheral zones. After TrypLE-treatment, the average radial strain significantly increased, caused mainly by conversion from compressive to tensile strain in the peripheral AL.

The structural and mechanical changes induced by TrypLE in the AL were similar to some features identified after several days of elevated IOP in the mouse experimental model of glaucoma [2,15]. For example, separation of astrocytes from their basement membrane and alterations in the astrocyte junctional complexes, as seen here, were features identified after a week of elevated IOP in a mouse model of glaucoma [2]. The separation observed with TEM was on the order of one hundred nanometers and may be smaller than what was seen *ex vivo* due to tissue dehydration during TEM preparation or due to the different resolution of *ex vivo* microscopy. The magnitudes of the strain before treatment in this study were similar to the magnitudes of strain in the control group of our previous study [15]. Furthermore, in the previous study, E_{rr} and E_{yy} significantly increased after three days of elevated IOP, as they did after TrypLE treatment. Moreover, the magnitudes of strain were similar after treatment with TrypLE and after three days of elevated IOP; for example, E_{yy} was 0.0297 ± 0.0194 after three days of elevated IOP and 0.029± 0.010 after treatment with TrypLE. Therefore, experimental treatment with TrypLE reproduced some of the microstructural and mechanical effects of short-term elevation of the IOP on the mouse AL, but in the absence of IOP elevation.

Author Manuscript Author Manuscript Author Manuscript Author Manuscript

There was further similarity between TrypLE-treatment and short-term IOP elevation effects in our PPS strain data. We confirmed that the strains in the connective tissues of the PPS of mouse eyes were much smaller than those of the cellular AL. There was, however, a significant increase in $E_{\theta\theta}$ of the PPS produced by TrypLE-treatment, while no significant change in E_{rr} occurred in the PPS, unlike in the adjoining AL. The astrocyte processes are interdigitated with the PPS collagen fibers where they meet up [2]. More work is needed to dissect the effect of the microstructure of the astrocyte processes on the mechanics in the PPS. The changes induced by TrypLE were similar to the changes due to 3-day IOP increase in the mouse PPS [15]. We demonstrated that the PPS collagen and elastin fibers are arranged in the mouse (as in human eyes) circumferentially, as would be likely to resist hoop stress produced by IOP [29]. In addition, this structural feature is disrupted by chronic IOP elevation, potentially altering PPS resistance to stress [30–32]. The responses of PPS and AL are likely to behave as a coupled unit, though the direction of their responses may depend on the relative contribution of the stresses presented by the overall sclera circumferentially and the trans-AL pressure difference between IOP and ON tissue pressure. In the human eyes, the mechanical coupling of the lamina cribrosa and the PPS has been shown experimentally [33] and in computational analyses of parameter interactions [34–36]. Midgett et al. reported a positive correlation of the $E_{\theta\theta}$ in the PPS to the $E_{\theta\theta}$ in the lamina cribrosa, and a positive correlation of the $E_{\theta\theta}$ in the PPS to the E_{rr} in the lamina cribrosa [33].

Some findings in our experimental TrypLE treatment differed from those in the findings in experimental models of glaucoma. For example, in serial tissue sections of six mouse eyes after bead-induced short-term IOP increase, the area of the AL increased somewhat and the spatial coverage of astrocytes decreased [3], while after TrypLE treatment these parameters were altered in the opposite directions, as measured by the area of GFP^{Astro} processes. The logical explanation for these differences is the swelling of the axonal compartment of the ONH with chronic IOP elevation, measured as 22% expansion by Ling et al. [3].

Other publications performed histological investigation of animal glaucoma models, mostly after an extended period of IOP increase. In the DBA/2 J mouse model of glaucoma, Cooper et al. examined the myelinated optic nerve, which is distal to the ONH, and reported retraction of astrocytic processes away from the center, but this included months of IOP increase, axon death, and probable long-term astrocyte remodeling. The study is important to understanding the Wallerian degeneration distal to the site of injury, but less directly applicable to the early biomechanical effects at the ONH [37]. We and others have shown in mouse and rat glaucoma models that astrocytic processes may extend novel, smaller processes [2,9] and that astrocytes alter the orientation of their processes to become more parallel to axons rather than in-plane across the ONH [10–12]. These effects are most likely a result of the sustained IOP elevation itself in these models. As such, they are not necessary to produce the strain change seen in our TrypLE-treated ONHs, which may therefore be more dependent on the loss of peripheral astrocyte connectivity.

A variety of features of the AL were either unchanged by TrypLE treatment or were not able to be measured in this study. TrypLE did not affect the area nor the width of astrocyte processes expressing GFP^{Astro} or labeled for F-actin. It would require biochemical analysis beyond the scope of this study to quantify cytoskeletal assembly. Observations made by

Author Manuscript Author Manuscript Author Manuscript Author Manuscript

LSM and by TEM did not find any decellularization due to treatment with TrypLE. The basement membrane in the AL was continuous in all samples examined with TEM. Cell-to-cell contacts in the AL were present and similar between samples treated with TrypLE and those treated with buffer.

The astrocytes of the ONH in larger mammals, including monkey and human eyes, have peripheral connections to the PPS similar to those of the mouse, but the human ONH is ten times larger and contains connective tissue beams on which astrocytes reside. As such, the mechanical contribution of astrocytes in normal and glaucomatous human eyes may differ in magnitude or type from those of the mouse. As described above, inflation studies by our laboratory in explanted, postmortem human ONH have qualitative similarities in AL and scleral strain to the mouse data. We and others have found, for example, that human explanted ONHs undergo changes in mechanical behavior after treatment with enzymes that affect their connective tissue, e.g. collagenase and chondroitinase [38–40]. It will be illuminating to carry out studies of the human ONH strain response using agents targeting astrocytes. Translational outcomes may be identified with such approaches.

There are some limitations to the data presented. At present, there are no methods to measure strain in the AL of the mouse in the living animal. To estimate strain in our *ex vivo* model requires maintaining a constant IOP while imaging the AL and PPS. This may represent conditions different from the eye in the living animal in which the IOP is fluctuating over time. The comparison of the mechanical response of the tissue after treatment to before treatment did not account for the alterations caused by unrecovered viscoelastic or plastic deformation. Such alterations may be induced by preconditioning of the tissue. The study also did not account for viscoelastic creep at the baseline pressure during the treatment step. In order to address these limitations, eyes were subjected to an identical inflation and treatment protocol, with buffer compared to TrypLE treatment. The strain difference in the buffer group may reflect the unrecovered deformation. In the astrocytic lamina, we estimated a 2% percent difference in the average principal strain, $(E_{max} + E_{min})/2$ between 2 quasi-static loading cycles in the buffer group. Compared to the differences between the first 2 loading cycles of the tree shrew sclera, our value was smaller than 21.30% reported by Bianco et al. and similar to 4% reported by Grytz et al. [41,42]. The strain difference in the TrypLE group exceeded the strain difference in the buffer group, but may include unrecoverable deformation. Eyes were subjected to 15-minute equilibration steps at each pressure in order to recover some of the deformation, as previously suggested [43,44]. However, another study with a greater sample size found that 15 min were insufficient for recovery of the scleral inflation response [41].

The mechanism of TrypLE proteolysis of the posterior components of the mouse eye, including the sclera, was not examined with biochemical assays [45]. Ling et al. analyzed antibody-labeled GFAP and phalloidin-labeled F-actin in cryopreserved tissue sections, reporting 62% and 68% coverage, respectively [3]. We analyzed images of cryopreserved tissue sections to obtain a similar area percentage of F-actin in the AL, which was 66% ± 2%. Immunolabeling for GFAP was not successfully applied to tissue sections, perhaps due to histological changes induced by the extended experimental protocol. Therefore, we analyzed the endogenous expression of green fluorescent protein (GFP^{Astro}) driven by

Author Manuscript Author Manuscript Author Manuscript Author Manuscript

the *Gfap* promoter in explanted eyes. The area coverage from the endogenous expression *ex vivo* was 38% smaller than the area coverage measured from antibody staining of cryopreserved tissues.

5. Conclusions

Treatment of explanted mouse eyes with TrypLE increased the structural compliance of the AL and caused the periphery of the AL to contract radially. DVC was used to correlate images before and after treatment with TrypLE or buffer, allowing both quantitative and spatially precise measurement of the changes in the astrocyte processes. TrypLE caused radial contraction of astrocyte processes in the periphery, which was also observed as a contraction of the AL area. TEM demonstrated a separation of astrocytes from their basement membrane, as well as thinning and loss of continuity of the junctional complexes. The magnitudes of E_{rr} and E_{yy} were similar after one-hour treatment with TrypLE to the magnitudes after three days of chronically elevated IOP in a previous study. The findings suggest that the reduction in the contact between AL and PPS contributes to the early increased mechanical response of the AL in the experimental model of glaucoma. Therefore, the detachment of astrocytic processes from the basement membrane adjacent to the scleral canal is an important remodeling mechanism in mouse glaucoma and may increase the mechanical vulnerability of the AL to elevated IOP.

Supplementary Material

Refer to Web version on PubMed Central for supplementary material.

Acknowledgements

This work was supported by the National Institutes of Health [grant numbers R01EY02120 and P30EY01765], by donors to the Glaucoma Center of Excellence, Wilmer Institute, Johns Hopkins University, and by the Provost's Undergraduate Research Award, Johns Hopkins University to M.N.

References

[1]. Sun D, Lye-Barthel M, Masland RH, Jakobs TC, The morphology and spatial arrangement of astrocytes in the optic nerve head of the mouse, J. Comp. Neurol (2009), doi:10.1002/cne.22058.

[2]. Quillen S, Schaub J, Quigley H, Pease M, Korneva A, Kimball E, Astrocyte responses to experimental glaucoma in mouse optic nerve head, PLoS ONE 15 (2020) e0238104, doi:10.1371/journal.pone.0238104. [PubMed: 32822415]

[3]. Ling YTT, Pease ME, Jefferys JL, Kimball EC, Quigley HA, Nguyen TD, Pressure-induced changes in astrocyte GFAP, actin, and nuclear morphology in mouse optic nerve, Investig. Opthalmology Vis. Sci 61 (2020) 14, doi:10.1167/iovs.61.11.14.

[4]. Howell GR, Libby RT, Jakobs TC, Smith RS, Phalan FC, Barter JW, Barbay JM, Marchant JK, Mahesh N, Porciatti V, Whitmore AV, Masland RH, John SWM, Axons of retinal ganglion cells are insulted in the optic nerve early in DBA/2 J glaucoma, J. Cell Biol 179 (2007) 1523–1537, doi:10.1083/jcb.200706181. [PubMed: 18158332]

[5]. Quigley HA, Addicks EM, Chronic experimental glaucoma in primates II. effect of extended intraocular pressure elevation on optic nerve head and axonal transport, Invest. Ophthalmol. Vis. Sci 19 (1980) 137–152. [PubMed: 6153173]

[6]. Quigley HA, Addicks EM, Green WR, Maumenee AE, Optic nerve damage in human glaucoma: II. the site of injury and susceptibility to damage, Arch. Ophthalmol 99 (1981) 635–649, doi:10.1001/archopht.1981.03930010635009. [PubMed: 6164357]

Author Manuscript Author Manuscript Author Manuscript Author Manuscript

[7]. Nguyen C, Midgett D, Kimball EC, Steinhart MR, Nguyen TD, Pease ME, Oglesby EN, Jefferys JL, Quigley HA, Measuring deformation in the mouse optic nerve head and peripapillary sclera, Investig. Ophthalmol. Vis. Sci 58 (2017) 721–733, doi:10.1167/iovs.16-20620. [PubMed: 28146237]

[8]. Pazos M, Yang H, Gardiner SK, Cepurna WO, Johnson EC, Morrison JC, Burgoyne CF, Expansions of the neurovascular scleral canal and contained optic nerve occur early in the hypertonic saline rat experimental glaucoma model, Exp. Eye Res 145 (2016) 173–186, doi:10.1016/j.exer.2015.10.014. [PubMed: 26500195]

[9]. Lye-Barthel M, Sun D, Jakobs TC, Morphology of astrocytes in a glaucomatous optic nerve, Investig. Ophthalmol. Vis. Sci 54 (2013) 909–917, doi:10.1167/iovs.12-10109. [PubMed: 23322566]

[10]. Tehrani S, Johnson EC, Cepurna WO, Morrison JC, Astrocyte processes label for filamentous actin and reorient early within the optic nerve head in a rat glaucoma model, Invest. Ophthalmol. Vis. Sci 55 (2014) 6945–6952, doi:10.1167/iovs.14-14969. [PubMed: 25257054]

[11]. Tehrani S, Davis L, Cepurna WO, Choe TE, Lozano DC, Monfared A, Cooper L, Cheng J, Johnson EC, Morrison JC, Astrocyte structural and molecular response to elevated intraocular pressure occurs rapidly and precedes axonal tubulin rearrangement within the optic nerve head in a rat model, PLoS ONE 11 (2016) 1–22, doi:10.1371/journal.pone.0167364.

[12]. Cooper ML, Collyer JW, Calkins DJ, Astrocyte remodeling without gliosis precedes optic nerve Axonopathy, Acta Neuropathol. Commun 6 (2018) 38, doi:10.1186/s40478-018-0542-0. [PubMed: 29747701]

[13]. Pena JDO, Agapova O, Gabelt BT, Levin LA, Lucarelli MJ, Kaufman PL, Hernandez MR, Increased elastin expression in astrocytes of the lamina cribrosa in response to elevated intraocular pressure, Investig. Ophthalmol. Vis. Sci 42 (2001) 2303–2314. [PubMed: 11527944]

[14]. Wang R, Seifert P, Jakobs TC, Astrocytes in the optic nerve head of glaucomatous mice display a characteristic reactive phenotype, Investig. Ophthalmol. Vis. Sci 58 (2017) 924–932, doi:10.1167/iovs.16-20571. [PubMed: 28170536]

[15]. Korneva A, Kimball EC, Jefferys JL, Quigley HA, Nguyen TD, Biomechanics of the optic nerve head and peripapillary sclera in a mouse model of glaucoma, J. R. Soc. Interface (2020) 17, doi:10.1098/rsif.2020.0708rsif20200708.

[16]. Alberts B, Johnson A, Lewis J, Raff M, Roberts K, Walter P, Molecular Biology of the Cell, W.W. Norton & Company, New York, 2007, doi:10.1201/9780203833445.

[17]. Zhao R, Boudou T, Wang WG, Chen CS, Reich DH, Decoupling cell and matrix mechanics in engineered microtissues using magnetically actuated micro-cantilevers, Adv. Mater 25 (2013) 1699–1705, doi:10.1002/adma.201203585. [PubMed: 23355085]

[18]. Branner S, Hastrup S, Recombinant trypsin-like protease, 5693520A, 1993.

[19]. Nielsen RI, Aaslyng DA, Jensen GW, Schneider P, Endoprotease from Fusarium Oxysporumdsm 2672 for use in detergents, 5288627A, 1988.

[20]. Tsuji K, Ojima M, Otabe K, Horie M, Koga H, Sekiya I, Muneta T, Effects of different cell-detaching methods on the viability and cell surface antigen expression of synovial mesenchymal stem cells, Cell Transplant 26 (2017) 1089–1102, doi:10.3727/096368917X694831. [PubMed: 28139195]

[21]. Manira M, Khairul Anuar K, Seet WT, Ahmad Irfan AW, Ng MH, Chua KH, Mohd Heikal MY, Aminuddin BS, Ruszymah BHI, Comparison of the effects between animal-derived trypsin and recombinant trypsin on human skin cells proliferation, gene and protein expression, Cell Tissue Bank 15 (2014) 41–49, doi:10.1007/s10561-013-9368-y. [PubMed: 23456438]

[22]. Zhuo L, Sun B, Zhang CL, Fine A, Chiu SY, Messing A, Live astrocytes visualized by green fluorescent protein in transgenic mice, Dev. Biol 187 (1997) 36–42, doi:10.1006/dbio.1997.8601. [PubMed: 9224672]

[23]. Otsu N, A threshold selection method from gray-level histograms, IEEE Trans. Syst. Man. Cybern 9 (1979) 62–66, doi:10.1109/TSMC.1979.4310076.

[24]. Ling YTT, Pressure-induced changes in astrocyte GFAP, actin, and nuclear morphology in mouse optic nerve, Github Repos (2020) https://www.doi.org/https://github.com/trayling/Morph_Analysis.

Author Manuscript Author Manuscript Author Manuscript Author Manuscript

[25]. Schrijver M, Kroon D−J, Hessian based Frangi vesselness filter, MATLAB Cent. File Exch (2019) https://www.mathworks.com/matlabcentral/fileexchange/24409-hessian-based-frangi-vesselness-filter. accessed May 12019

[26]. Schindelin J, Arganda-Carreras I, Frise E, Kaynig V, Longair M, Pietzsch T, Preibisch S, Rueden C, Saalfeld S, Schmid B, Tinevez JY, White DJ, Hartenstein V, Eliceiri K, Tomancak P, Cardona A, Fiji: an open-source platform for biological-image analysis, Nat. Methods 9 (2012) 676–682, doi:10.1038/nmeth.2019. [PubMed: 22743772]

[27]. Bar-Kochba E, Toyjanova J, Andrews E, Kim K−S, Franck C, A fast iterative digital volume correlation algorithm for large deformations, Exp. Mech 55 (2015) 261–274, doi:10.1007/s11340-014-9874-2.

[28]. Bar-Kochba E, Toyjanova J, Andrews E, Kim K−S, Franck C, A fast iterative digital volume correlation algorithm for large deformations, Github Repos (2019) https://www.doi.org/https://github.com/FranckLab/FIDVC.

[29]. Pijanka JK, Kimball EC, Pease ME, Abass A, Sorensen T, Nguyen TD, Quigley HA, Boote C, Changes in scleral collagen organization in murine chronic experimental glaucoma, Invest. Ophthalmol. Vis. Sci 55 (2014) 6554–6564, doi:10.1167/iovs.14-15047. [PubMed: 25228540]

[30]. Pijanka JK, Coudrillier B, Ziegler K, Sorensen T, Meek KM, Nguyen TD, Quigley HA, Boote C, Quantitative mapping of collagen fiber orientation in non-glaucoma and glaucoma posterior human sclerae, Investig. Ophthalmol. Vis. Sci 53 (2012) 5258–5270, doi:10.1167/iovs.12-9705. [PubMed: 22786908]

[31]. Coudrillier B, Pijanka JK, Jefferys JL, Goel A, Quigley HA, Boote C, Nguyen TD, Glaucoma-related changes in the mechanical properties and collagen micro-architecture of the human sclera, PLoS ONE 10 (2015) 1–21, doi:10.1371/journal.pone.0131396.

[32]. Pijanka JK, Spang MT, Sorensen T, Liu J, Nguyen TD, Quigley HA, Boote C, Depth-dependent changes in collagen organization in the human peripapillary sclera, PLoS ONE 10 (2015) 1–17, doi:10.1371/journal.pone.0118648.

[33]. Midgett DE, Jefferys JL, Quigley HA, Nguyen TD, The inflation response of the human lamina cribrosa and sclera: analysis of deformation and interaction, Acta Biomater 106 (2020) 225–241, doi:10.1016/j.actbio.2020.01.049. [PubMed: 32044458]

[34]. Sigal IA, Yang H, Roberts MD, Grimm JL, Burgoyne CF, Demirel S, Downs JC, IOP-induced lamina cribrosa deformation and scleral canal expansion: independent or related? Investig. Ophthalmol. Vis. Sci 52 (2011) 9023–9032, doi:10.1167/iovs.11-8183. [PubMed: 21989723]

[35]. Sigal IA, Flanagan JG, Ethier CR, Factors influencing optic nerve head biomechanics, Investig. Opthalmology Vis. Sci 46 (2005) 4189, doi:10.1167/iovs.05-0541.

[36]. Coudrillier B, Boote C, Quigley HA, Nguyen TD, Scleral anisotropy and its effects on the mechanical response of the optic nerve head, Biomech. Model. Mechanobiol 12 (2013) 941–963, doi:10.1007/s10237-012-0455-y. [PubMed: 23188256]

[37]. Cooper ML, Crish SD, Inman DM, Horner PJ, Calkins DJ, Early astrocyte redistribution in the optic nerve precedes axonopathy in the DBA/2 J mouse model of glaucoma, Exp. Eye Res 150 (2016) 22–33, doi:10.1016/j.exer.2015.11.016. [PubMed: 26646560]

[38]. Spoerl E, Boehm AG, Pillunat LE, The influence of various substances on the biomechanical behavior of lamina cribrosa and peripapillary sclera, Investig. Opthalmology Vis. Sci 46 (2005) 1286, doi:10.1167/iovs.04-0978.

[39]. Murienne BJ, Chen ML, Quigley HA, Nguyen TD, The contribution of glycosaminoglycans to the mechanical behaviour of the posterior human sclera, J. R. Soc. Interface (2016) 13, doi:10.1098/rsif.2016.0367.

[40]. Midgett DE, Jefferys JL, Quigley HA, Nguyen TD, The contribution of sulfated glycosaminoglycans to the inflation response of the human optic nerve head, Invest. Ophthalmol. Vis. Sci 59 (2018) 3144–3154, doi:10.1167/iovs.18-23845. [PubMed: 30025126]

[41]. Bianco G, Levy AM, Grytz R, Fazio MA, Effect of different preconditioning protocols on the viscoelastic inflation response of the posterior sclera, Acta Biomater 128 (2021) 332–345, doi:10.1016/j.actbio.2021.04.042. [PubMed: 33932581]

Author Manuscript Author Manuscript Author Manuscript Author Manuscript

[42]. Grytz R, Siegwart JT, Changing material properties of the tree shrew sclera during minus lens compensation and recovery, Investig. Opthalmology Vis. Sci 56 (2015) 2065, doi:10.1167/iovs.14-15352.

[43]. Myers KM, Coudrillier B, Boyce BL, Nguyen TD, The inflation response of the posterior bovine sclera, Acta Biomater 6 (2010) 4327–4335, doi:10.1016/j.actbio.2010.06.007. [PubMed: 20558331]

[44]. Tonge TK, Murienne BJ, Coudrillier B, Alexander S, Rothkopf W, Nguyen TD, Minimal preconditioning effects observed for inflation tests of planar tissues, J. Biomech. Eng (2013) 135, doi:10.1115/1.4025105.

[45]. Schor SL, Court J, Different mechanisms in the attachment of cells to native and denatured collagen, J. Cell Sci 38 (1979) 267–281, doi:10.1242/jcs.38.1.267. [PubMed: 521466]

Author Manuscript Author Manuscript Author Manuscript Author Manuscript

Statement of significance

Astrocytes of the optic nerve of the eye spread out from edge to edge across the optic nerve in a region referred to as the astrocytic lamina. In an experimental model of glaucoma caused by elevated eye-pressure, there is disruption of the connections between astrocytes and the edge of the astrocytic lamina. We caused a similar event in the lamina by incubating explanted mouse eyes with an enzyme. Disruption of the astrocyte connections to the edge of their tissue caused the tissue to stretch more when we increased the eye-pressure, compared to the control tissue. This work is the first on the tissue of the optic nerve to demonstrate the importance of cell connections in preventing the over-stretching of the astrocytic lamina.

Author Manuscript Author Manuscript Author Manuscript Author Manuscript

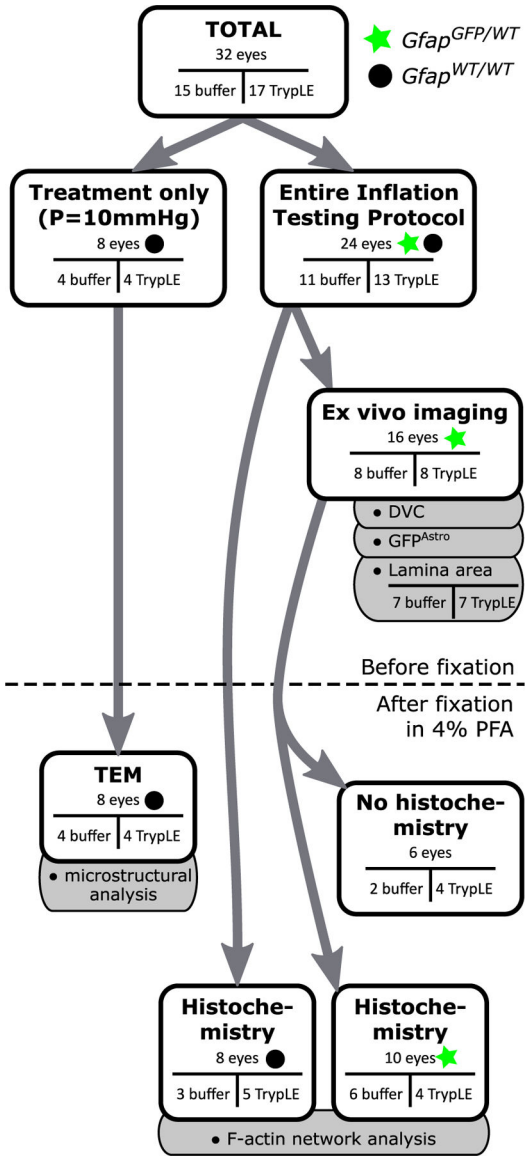

Fig. 1.

Overview of the experimental protocol and the sample sizes of the experiment. Both $Gfap^{GFP/WT}$ (green star) and $Gfap^{WT/WT}$ (black circle) animals were used. Arrows show the breakdown of the analysis performed on the same eye. Gray tabs indicate the analyses on images from the respective methods. A schematic of the entire inflation protocol is in Fig. 2. Out of 16 eyes, only 7 from the buffer group and 7 from the TrypLE group had z-stacks of the AL and PPS which were able to be used for the analysis of the lamina area (c.f. Section 2.5). The methods which were carried out on eyes after they were fixed are drawn below the dashed line. The analysis of the F-actin process network was on eyes pooled from mice of both genotypes. (For interpretation of the references to colour in this figure legend, the reader is referred to the web version of this article.)

Author Manuscript Author Manuscript Author Manuscript Author Manuscript

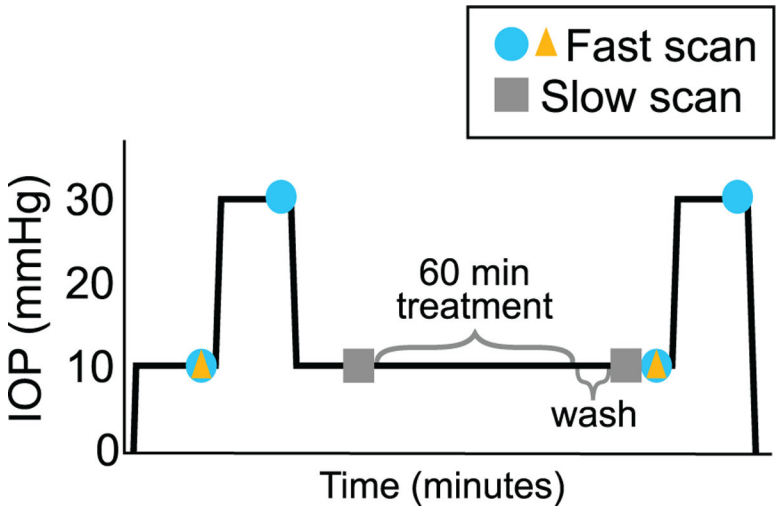

Fig. 2.

Experimental protocol showing the IOP on the y-axis and the approximate time on the x-axis. Equilibration for 15 min followed each change in pressure. Z-stack scans were collected at the times indicated on the schematic for the subset of eyes which were placed under the scanning microscope. Fast scans were used in the analysis of the lamina area and the analysis of deformation of the AL by treatment (yellow triangles), and for the strain response (blue circles). Slow scans (gray squares) were used for the analysis of GFP^{Astro} process network. (For interpretation of the references to colour in this figure legend, the reader is referred to the web version of this article.)

Author Manuscript Author Manuscript Author Manuscript Author Manuscript

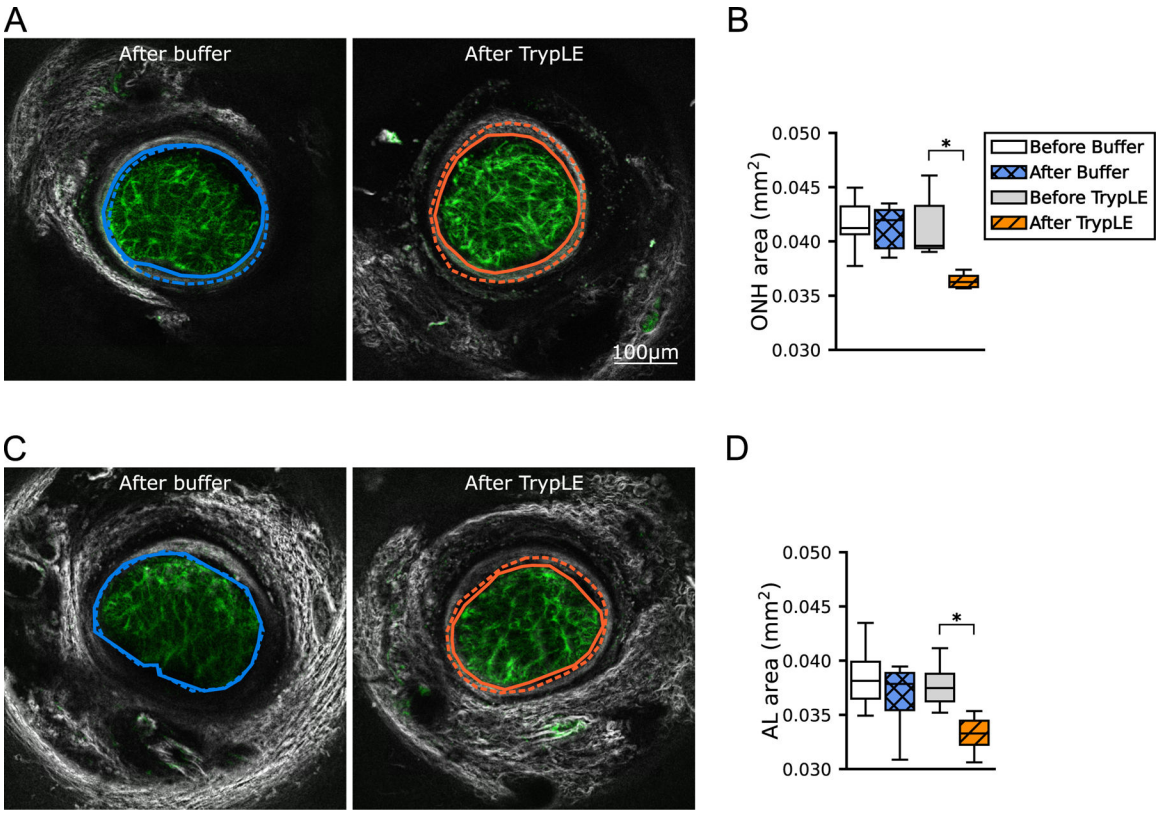

Fig. 3.

ONH and AL areas. Numerical values are in Table 1. Representative z-slices from fast scans taken after the treatment and wash steps. The black and white PPS (SHG and TPF) image was merged with the green GFP^{Astro} (TPF) image. (A) The ONH area was outlined along the inner border of the connective tissue of the pia mater and PPS after treatment (solid line) and before treatment (dashed line, image not shown). (C) The AL was outlined along the outer boundary of the GFP^{Astro} signal. (B, D) Boxplots of the areas enclosed by these outlines Areas were smaller after TrypLE treatment (solid orange line) than before treatment (dashed orange line) ($n = 7$, paired, $p<0.05$). Boxplots: the interquartile range of areas of $n = 7$ samples per group, the line marks the median, and whiskers are drawn by Tukey's method. $^{*}p<0.05$ from Wilcoxon signed rank tests. Scale Bar=100 μm. (For interpretation of the references to colour in this figure legend, the reader is referred to the web version of this article.)

Author Manuscript Author Manuscript Author Manuscript Author Manuscript

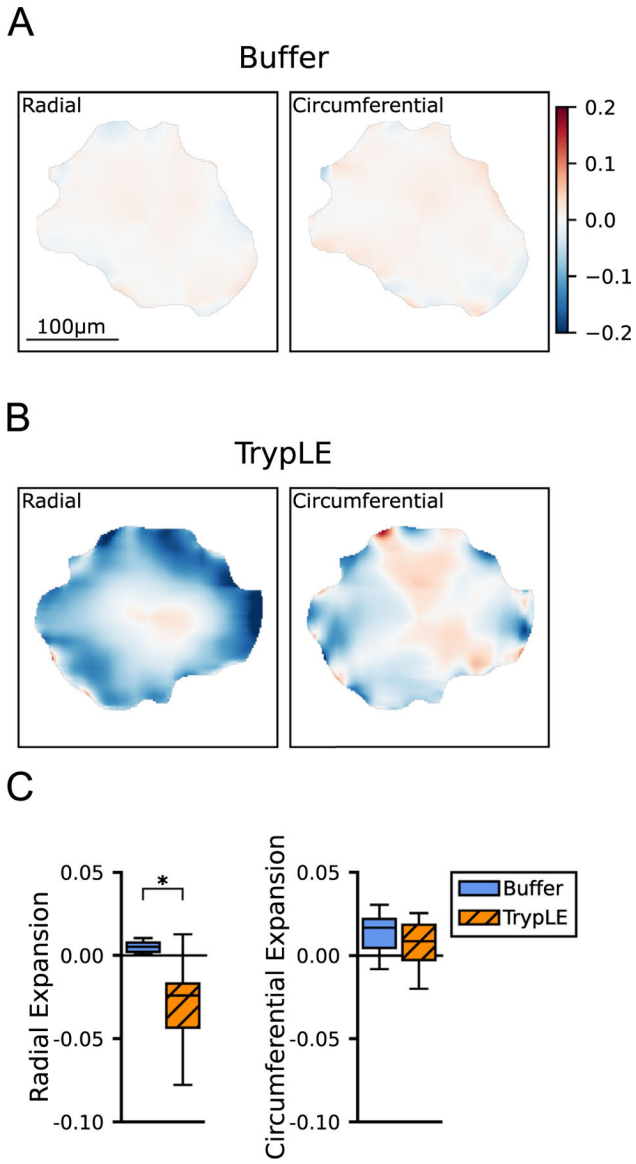

Fig. 4.

Color contours of the DVC results showing deformation of the AL due to treatment. Numerical values are in Table 2. (A) Radial and circumferential expansion of a sample due to treatment with buffer and (B) of another sample due to treatment with TrypLE. Color scale minimum indicates contraction of 0.20 (blue, negative expansion) and the maximum indicates expansion of 0.20 (red, positive expansion). There was significant radial contraction (deep blue) in the periphery and rim of the AL due to treatment with TrypLE (B). (C) Boxplots of the radial and circumferential expansion due to treatment ($n = 8$ per group). Statistical significance of $p<0.05$ by Mann-Whitney U test. Scale Bar=100 μm. (For interpretation of the references to colour in this figure legend, the reader is referred to the web version of this article.)

Author Manuscript Author Manuscript Author Manuscript Author Manuscript

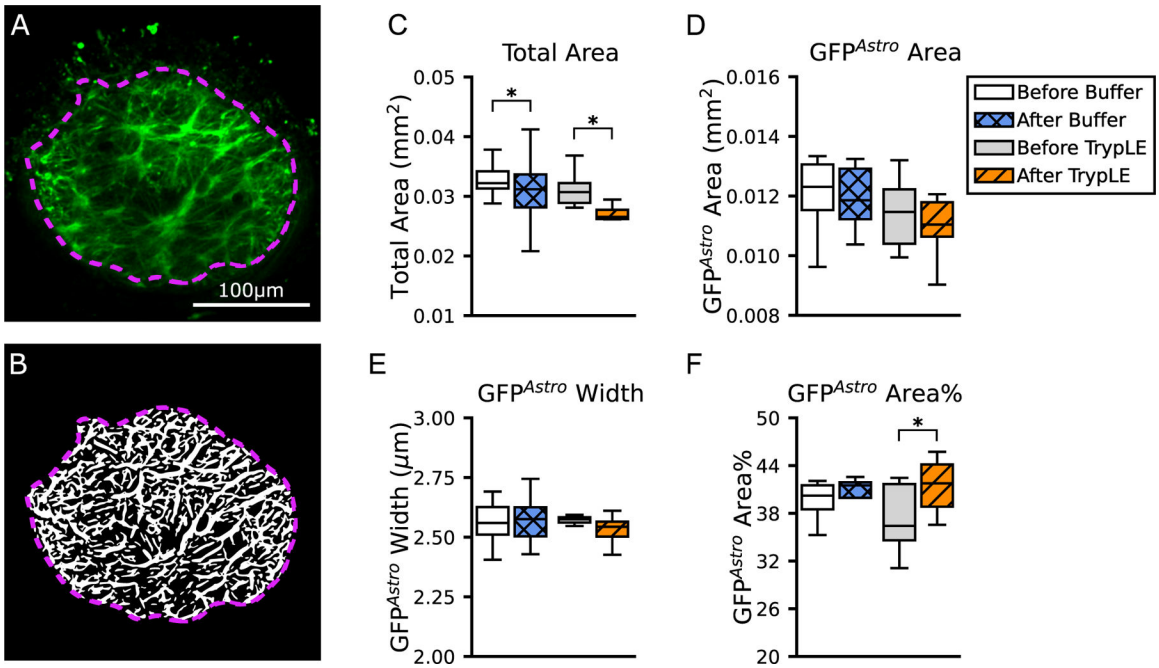

Fig. 5.

Characterization of the processes expressing GFP^{Astro} in the AL. Numerical values are in Table 3. (A) One representative z-slice from a slow scan taken before the treatment with buffer. Green is the TPF of the GFP^{Astro} image. The image was enhanced and processed by the network analysis algorithm in order to detect processes, shown in white in the (B) binarized image. The total AL area is marked by the violet dashed line. (C) Boxplots of the total AL area show that it was smaller after treatment with buffer ($p = 0.03$) and even more dramatically after treatment with TrypLE ($p = 0.0001$). (D) Boxplots of the area of GFP^{Astro} processes, (E) the GFP^{Astro} process width, and (F) the GFP^{Astro} Area%. Statistical significance is from Wilcoxon signed rank tests, with $^{*}p<0.05$ ($n = 8$ per group). Scale Bar=100 μm.

Author Manuscript Author Manuscript Author Manuscript Author Manuscript

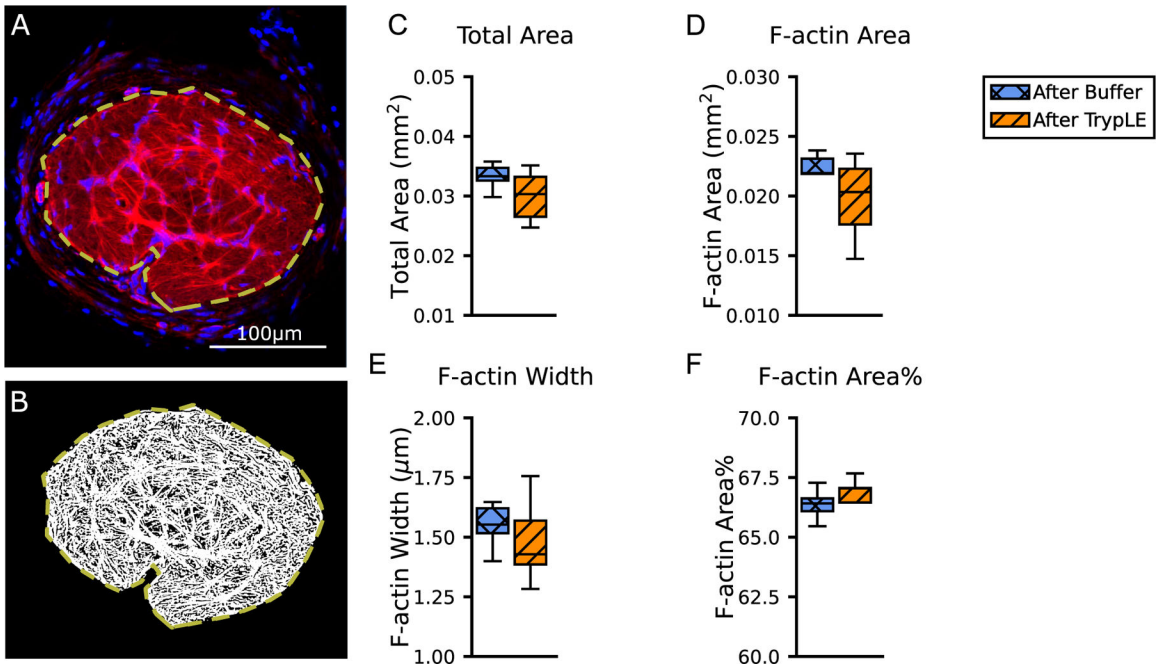

Fig. 6.

Characterization of the actin network in the AL. Numerical values are in Table 4. (A) One representative image from the TrypLE group, from histochemistry labeling for F-actin (phalloidin, red) and nuclei (DAPI, blue). The image was enhanced and processed by the network analysis algorithm in order to detect processes, shown in white in the (B) binarized image. The total area of AL is marked by the yellow dashed line. (C) Boxplots of the total area, (D) area of F-actin processes, (E) F-actin process width, and (F) F-actin area% (n = 9 buffer, n = 9 TrypLE). Mann-Whitney U tests did not find statistical significance (p>0.05) between the buffer and TrypLE groups. Scale Bar=100 μm. (For interpretation of the references to colour in this figure legend, the reader is referred to the web version of this article.)

Author Manuscript Author Manuscript Author Manuscript Author Manuscript

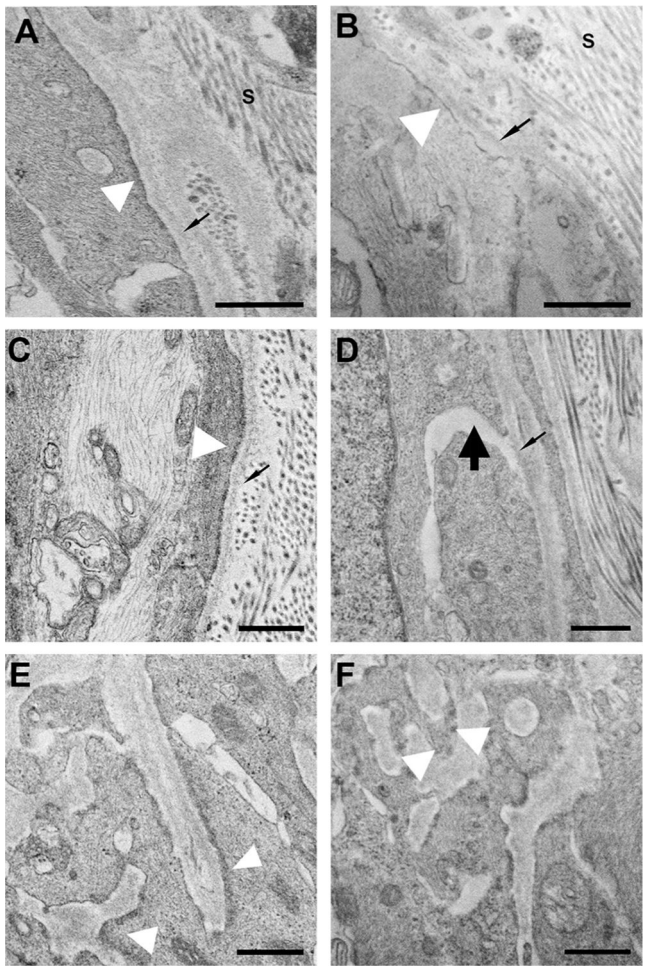

Fig. 7.

TEM images comparing buffer-treated (A,C,E) and TrypLE-treated tissue (B,D,F). The 3 rows illustrate examples of the 3 astrocyte ultrastructural characteristics graded in masked fashion: (A,B) the thickness of junctional complexes (white arrowhead); (C,D) the proximity of the astrocyte cell membrane to its basement membrane (thin black arrow marks basement membrane); and (E,F) the continuity of junctional complexes. (A) normal, thick junctional complexes (grade 1); (B) thinned complexes (grade 4); (C) uniform, minimal space between cell membrane and basement membrane (grade 1); (D) wide spaces between cells and basement membrane (grade 4, thick black arrow); (E) continuous junctional complexes (grade 1); (F) intermittent junctional complexes (grade 4). *s* = sclera. Scale bars=500 nm.

Author Manuscript Author Manuscript Author Manuscript Author Manuscript

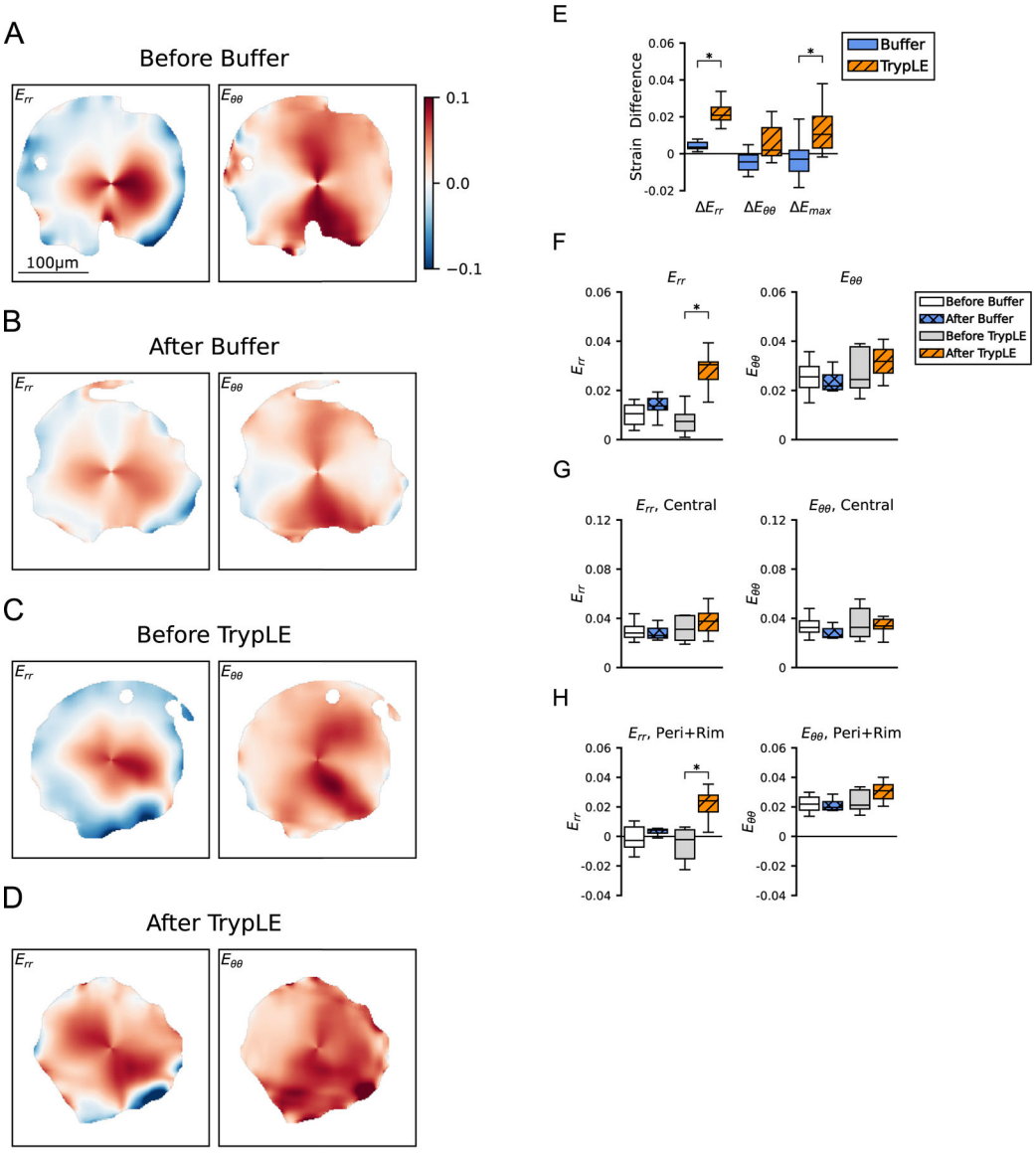

Fig. 8.

Strain response of the AL due to IOP increase from 10 to 30 mmHg, before and after treatment. Numerical values are in Table 5. Representative color contours of E_{rr} and $E_{\theta\theta}$. Strain response (A) before treatment with buffer, (B) after treatment with buffer, (C) before treatment with TrypLE, and (D) after treatment with TrypLE. E_{rr} after treatment with TrypLE (D) was significantly more tensile (redder) than before treatment (C). (E) Boxplots of the strain differences, e.g., $\Delta E_{rr} = E_{rr,\,after} - E_{rr,\,before}$, for the buffer and TrypLE treatment groups. The strain differences ΔE_{rr} and ΔE_{max} due to TrypLE were statistically greater than the strain differences due to buffer ($n = 8$ per group, $p \leq 0.03$). Boxplots of E_{rr} and $E_{\theta\theta}$ were averaged for (F) the entire AL area, (F) the central region, and (G) the combined peripheral and rim regions. Statistical significance, $^{*}p<0.05$, was from Wilcoxon signed rank tests. Scale Bar=100 μm. (For interpretation of the references to colour in this figure legend, the reader is referred to the web version of this article.)

Author Manuscript Author Manuscript Author Manuscript Author Manuscript

Table 1

ONH and AL areas. Fig. 3 shows representative measurements. TrypLE caused a contraction of the ONH and AL areas (n = 7 buffer group, n = 7 TrypLE group). P-values are from Wilcoxon signed rank tests comparing areas before and after treatment. Areas are in mm^2 , mean ± std.

	Group	Before	After	Percent Difference	*p-value* Before vs. After
ONH area	Buffer	0.041 ± 0.002	0.043 ± 0.005	3.4% ± 10.4%	0.81
	TrypLE	0.041 ± 0.003	0.037 ± 0.004	−9.9% ± 5.8%	**0.03**
AL area	Buffer	0.037 ± 0.004	0.037± 0.004	−0.3% ± 2.4%	>0.99
	TrypLE	0.037 ± 0.003	0.033 ± 0.002	−10.8% ± 6.1%	**0.02**

Acta Biomater. Author manuscript; available in PMC 2024 June 01.

Author Manuscript Author Manuscript Author Manuscript Author Manuscript

Table 2

Deformation of the AL due to treatment with buffer or TrypLE (n = 8 per group). Fig. 4. shows representative results from DVC. Radial and circumferential expansion defined by E_{rr} and $E_{\theta\theta}$, respectively, calculated from DVC of image volumes taken at 10 mmHg before and after treatment. Expansion was averaged in the whole specimen, or regionally in the central and in the combined peripheral and rim regions (Peri + Rim). The radial expansion was negative (i.e., contraction) and significantly smaller (i.e., more contraction) due to TrypLE than buffer ($p \leq 0.007$). P-values are from Mann-Whitney U tests comparing the buffer and TrypLE groups, $p<0.05$ is significant. Values are mean ± std.

	Region	**Group**	**Expansion**	***p*-value**
Radial Expansion	Whole	Buffer	0.005 ± 0.007	**0.004**
		TrypLE	−0.029 ± 0.027	
	Central	Buffer	0.010 ± 0.014	0.44
		TrypLE	0.001 ± 0.021	
	Peri + Rim	Buffer	0.002 ± 0.016	**0.007**
		TrypLE	−0.044 ± 0.038	
Circumferential Expansion	Whole	Buffer	0.014 ± 0.013	0.3
		TrypLE	0.006 ± 0.017	
	Central	Buffer	0.016 ± 0.017	0.38
		TrypLE	0.012 ± 0.010	
	Peri + Rim	Buffer	0.012 ± 0.011	0.51
		TrypLE	0.002 ± 0.023	

Author Manuscript Author Manuscript Author Manuscript Author Manuscript

Table 3

Characterization of the processes expressing GFP^{Astro} in the AL. Fig. 5. shows representative images. The GFP^{Astro} area% increased after treatment with TrypLE (n = 8, p = 0.006). Wilcoxon signed rank tests compared values before to after treatment and Mann Whitney U tests compared values after buffer to those after TrypLE (n = 8 per group), p<0.05 is significant. Values are mean ± std.

	Group	Before	After	*p-value* Before vs. After	*p-value* After Buffer vs. After TrypLE
Area occupied by GFP^{Astro}	Buffer	0.013 ± 0.003	0.012 ± 0.002	0.07	0.49
processes (mm^2)	TrypLE	0.011 ± 0.001	0.011 ± 0.001	0.39	
Total AL area (mm^2)	Buffer	**0.033 ± 0.007**	**0.031 ± 0.006**	**0.03**	0.15
	TrypLE	**0.031 ± 0.003**	**0.027 ± 0.002**	**0.0001**	
GFP^{Astro} area%	Buffer	38.8% ± 4.1%	39.4% ± 5.0%	0.77	0.55
	TrypLE	**37.2% ± 4.3%**	**41.5% ± 3.3%**	**0.0006**	
GFP^{Astro} process width (μm)	Buffer	2.56 ± 0.10	2.57 ± 0.10	0.85	0.52
	TrypLE	2.57 ± 0.03	2.53 ± 0.06	0.25	

Acta Biomater. Author manuscript; available in PMC 2024 June 01.

Author Manuscript Author Manuscript Author Manuscript Author Manuscript

Table 4

Characterization of the actin network in the AL. Fig. 6. shows representative images. All measures of the F-actin processes were similar between eyes treated with TrypLE and eyes treated with buffer. P-values are from the Mann-Whitney U test. Values are mean ± std.

	Group	After	*p-value* After Buffer vs. After TrypLE
Area occupied by F-actin processes (mm^2)	Buffer	0.022 ± 0.002	0.14
	TrypLE	0.020 ± 0.003	
Total area (mm^2)	Buffer	0.033 ± 0.003	0.09
	TrypLE	0.030 ± 0.004	
F-actin area%	Buffer	66.3% ± 0.6%	0.20
	TrypLE	65.8% ± 3.2%	
F-actin process width (μm)	Buffer	1.53 ± 0.11	0.45
	TrypLE	1.47 ± 0.15	

Author Manuscript Author Manuscript Author Manuscript Author Manuscript

Acta Biomater. Author manuscript; available in PMC 2024 June 01.

Table 5

Strain response of the AL due to IOP increase from 10 to 30 mmHg, before and after treatment. Fig. 8. shows representative results from DVC. Three normal strain components (E_{rr}, E_{xx}, E_{yy}) and E_{max} were significantly greater after treatment with TrypLE than before ($n = 8$, $p \leq 0.04$). Values are mean ± std, and p-values are from Wilcoxon signed rank test comparing the values before vs. after treatment within one treatment group ($n = 8$ per group).

	Group	Before	After	*p-value* Before vs. After
E_{rr}	Buffer	0.010 ± 0.005	0.014 ± 0.004	0.08
	TrypLE	**0.006 ± 0.008**	**0.028 ± 0.009**	**0.01**
$E_{\theta\theta}$	Buffer	0.028 ± 0.014	0.026 ± 0.009	0.38
	TrypLE	0.027 ± 0.009	0.033 ± 0.010	0.36
$E_{r\theta}$	Buffer	0.000 ± 0.001	0.001 ± 0.001	0.38
	TrypLE	0.000 ± 0.002	0.000 ± 0.002	0.92
E_{xx}	Buffer	0.028 ± 0.011	0.027 ± 0.010	0.64
	TrypLE	**0.023 ± 0.007**	**0.032 ± 0.007**	**0.04**
E_{yy}	Buffer	0.011 ± 0.007	0.012 ± 0.006	0.11
	TrypLE	**0.011 ± 0.007**	**0.029 ± 0.010**	**0.01**
E_{xy}	Buffer	0.002 ± 0.009	0.003 ± 0.008	0.74
	TrypLE	0.004 ± 0.006	0.006 ± 0.008	0.55
E_{max}	Buffer	0.042 ± 0.018	0.040 ± 0.012	0.48
	TrypLE	**0.038 ± 0.009**	**0.051 ± 0.012**	**0.04**
E_{min}	Buffer	−0.003 ± 0.006	0.000 ± 0.005	0.20
	TrypLE	**−0.004 ± 0.008**	**0.010 ± 0.007**	**0.01**
γ_{max}	Buffer	0.023 ± 0.011	0.020 ± 0.006	0.46
	TrypLE	0.021 ± 0.006	0.020 ± 0.005	0.46
E_{zz}	Buffer	0.000 ± 0.003	0.000 ± 0.002	0.98
	TrypLE	0.001 ± 0.007	−0.002 ± 0.005	0.31

Author Manuscript Author Manuscript Author Manuscript Author Manuscript

Table 6

Strain response of the PPS due to IOP increase from 10 to 30 mmHg, before and after treatment. The principal strains (E_{max}, E_{min}, γ_{max}) and $E_{\theta\theta}$ were significantly greater after treatment with TrypLE than before ($n = 8$, $p \leq 0.02$). Values are mean ± std, and p-values are from Wilcoxon signed rank test comparing the values before vs. after treatment within one treatment group ($n = 8$ per group).

	Group	Before	After	*p-value* Before vs. After
E_{rr}	Buffer	0.0001 ± 0.0035	−0.0006 ± 0.0041	0.38
	TrypLE	0.0003 ± 0.0064	−0.0009 ± 0.0056	0.20
$E_{\theta\theta}$	Buffer	0.0037 ± 0.0014	0.0047 ± 0.0036	0.72
	TrypLE	**0.0049 ± 0.0039**	**0.0068 ± 0.0053**	**0.02**
$E_{r\theta}$	Buffer	0.0008 ± 0.0035	0.0009 ± 0.0019	0.46
	TrypLE	0.0005 ± 0.0018	0.0006 ± 0.0012	0.30
E_{xx}	Buffer	0.0003 ± 0.0020	−0.0002 ± 0.0034	0.53
	TrypLE	−0.0008 ± 0.0058	−0.0008 ± 0.0034	0.95
E_{yy}	Buffer	0.0034 ± 0.0020	0.0043 ± 0.0037	0.71
	TrypLE	0.0060 ± 0.0033	0.0067 ± 0.0028	0.40
E_{xy}	Buffer	−0.0009 ± 0.0020	0.0001 ± 0.0025	0.64
	TrypLE	−0.0011 ± 0.0011	−0.0011 ± 0.0020	0.97
E_{max}	Buffer	0.0141 ± 0.0092	0.0145 ± 0.0071	0.84
	TrypLE	**0.0149 ± 0.0073**	**0.0192 ± 0.0107**	**0.02**
E_{min}	Buffer	−0.0103 ± 0.0092	−0.0104 ± 0.0028	0.20
	TrypLE	**−0.0096 ± 0.0090**	**−0.0133 ± 0.0094**	**0.04**
γ_{max}	Buffer	0.0122 ± 0.0091	0.0124± 0.0046	1.00
	TrypLE	**0.0123 ± 0.0079**	**0.0162 ± 0.0098**	**0.01**

Acta Biomater. Author manuscript; available in PMC 2024 June 01.